

# A high-performance supercapacitor-battery hybrid energy storage device based on graphene-enhanced electrode materials with ultrahigh energy density†

Cite this: *Energy Environ. Sci.*, 2013, **6**, 1623

Fan Zhang, Tengfei Zhang, Xi Yang, Long Zhang, Kai Leng, Yi Huang and Yongsheng Chen\*

In pursuing higher energy density with no sacrifice of power density, a supercapacitor-battery hybrid energy storage device—combining an electrochemical double layer capacitance (EDLC) type positive electrode with a Li-ion battery type negative electrode—has been designed and fabricated. Graphene is introduced to both electrodes: an Fe<sub>3</sub>O<sub>4</sub>/graphene (Fe<sub>3</sub>O<sub>4</sub>/G) nanocomposite with high specific capacity as negative electrode material, and a graphene-based three-dimensional porous carbon material (3DGraphene) with high surface area (~3355 m<sup>2</sup> g<sup>-1</sup>) as positive electrode material. The Fe<sub>3</sub>O<sub>4</sub>/G nanocomposite shows a high reversible specific capacity exceeding 1000 mA h g<sup>-1</sup> at 90 mA g<sup>-1</sup> and remaining at 704 mA h g<sup>-1</sup> at 2700 mA g<sup>-1</sup>, as well as excellent rate capability and improved cycle stability. Meanwhile the 3DGraphene positive electrode also displays great electrochemical performance. With these two graphene-enhanced electrode materials and using the best recommended industry evaluation method, the hybrid supercapacitor Fe<sub>3</sub>O<sub>4</sub>/G//3DGraphene demonstrates an ultrahigh energy density of 147 W h kg<sup>-1</sup> (power density of 150 W kg<sup>-1</sup>), which also remains of 86 W h kg<sup>-1</sup> even at high power density of 2587 W kg<sup>-1</sup>, so far the highest value of the reported hybrid supercapacitors. Furthermore, the energy density of the hybrid supercapacitor is comparable to lithium ion batteries, and the power density also reaches that of symmetric supercapacitors, indicating that the hybrid supercapacitor could be a very promising novel energy storage system for fast and efficient energy storage in the future.

Received 13th February 2013  
Accepted 18th March 2013

DOI: 10.1039/c3ee40509e

[www.rsc.org/ees](http://www.rsc.org/ees)

## Broader context

Supercapacitors with excellent power density and lithium ion batteries with high energy density are currently both considered to be novel, environmentally friendly and high-performance energy storage devices. Nevertheless, in view of numerous applications of electronic devices and hybrid electric vehicles, there has been great demand for high-performance energy storage devices with both high energy density and power density. To solve this problem, a novel supercapacitor–battery hybrid energy storage system, the hybrid supercapacitor, has emerged in recent years, composed of a capacitor-type electrode and a lithium ion battery-type electrode thus are expected to possess the best features of both supercapacitors and batteries. Although most works have reported fabrication of such devices based on activated carbon as a supercapacitor-type positive electrode material, and Li<sub>4</sub>Ti<sub>5</sub>O<sub>12</sub>, graphite or metal oxides as the battery-type negative electrode material, the poor conductivity, low capacity or instability of these materials have limited the electrochemical performance of the devices. Thus in this work, we designed a hybrid supercapacitor using cost-effective graphene-enhanced Fe<sub>3</sub>O<sub>4</sub>/G negative and 3DGraphene positive electrode materials for improving both the energy and power density performance, which exhibits an ultrahigh energy density of 147 W h kg<sup>-1</sup> with good rate performance, so far the highest value of the reported hybrid supercapacitors.

## Introduction

Energy storage has become a global concern in modern society, and high-performance energy storage devices is under great demand. Among various electrical energy storage devices (*e.g.*, lead–acid batteries, nickel–metal hydride batteries, lithium ion batteries, and supercapacitors), lithium ion batteries (LIBs) with high energy density and supercapacitors (SCs) with excellent power density are currently considered to be two excellent candidates as novel, environmental-friendly, low-cost, and high-performance energy storage devices to meet the needs of

Key Laboratory of Functional Polymer Materials and Centre for Nanoscale Science and Technology, Institute of Polymer Chemistry, College of Chemistry, Nankai University, 300071, Tianjin, China. E-mail: [yschen99@nankai.edu.cn](mailto:yschen99@nankai.edu.cn)

† Electronic supplementary information (ESI) available: Figures of TGA curve of Fe<sub>3</sub>O<sub>4</sub>/G composite, XRD profile of as-prepared Fe<sub>3</sub>O<sub>4</sub>, SEM and TEM images of as-prepared Fe<sub>3</sub>O<sub>4</sub>, N<sub>2</sub> adsorption–desorption results, characterization of 3DGraphene material, performance of SUAC-based supercapacitor and 3DGraphene-based half cell, and Ragone plots of Fe<sub>3</sub>O<sub>4</sub>/G//3DGraphene hybrid devices with different mass ratios of positive against negative materials. See DOI: 10.1039/c3ee40509e

increasing demand. The LIBs commonly can store a large amount of energy as high as 150–200 W h kg<sup>-1</sup>, but are confined by their low power density (below 1000 W kg<sup>-1</sup>) and poor cycle life (usually less than 1000 cycles).<sup>1</sup> In contrast, supercapacitors can provide much higher power density (10 kW kg<sup>-1</sup>), long cycle life (exceeding 1 × 10<sup>5</sup> cycles) and fast charge–discharge processes (within seconds),<sup>2</sup> but suffer from much lower energy density (only 5–10 W h kg<sup>-1</sup>).<sup>3</sup> However, in view of numerous applications of electronic devices and hybrid electric vehicles, there has been great and urgent demand for high-performance energy storage devices with both high energy density and power density.

With a combination of the fast charging rate of SCs and the high energy density of LIBs, a novel supercapacitor–battery hybrid energy storage system, also called hybrid supercapacitor (HSC) has emerged, which is expected to possess the best features of both SCs and LIBs.<sup>4</sup> HSCs are composed of a capacitor-type electrode and a lithium ion battery-type electrode in a Li salt containing organic electrolyte. The combination of two different types of electrode would result in the storage of more energy due to the much wider working voltage window of the organic electrolyte and the great specific capacity of the battery-type electrode.<sup>5</sup> The charge–discharge rate can still remain at a fast degree (charging in minutes) because of the EDLC type electrode. Therefore, the key to fabricating a high-performance HSC is to couple both appropriate electrode materials in the device. On one hand, activated carbon (AC) is commonly used as a typical electrochemical double layer capacitance (EDLC) positive electrode material,<sup>6,7</sup> while some novel carbon-based materials with extraordinary properties have recently been reported to improve the EDLC performances.<sup>8–11</sup> On the other hand, Li<sub>4</sub>Ti<sub>5</sub>O<sub>12</sub> (LTO),<sup>5,12</sup> graphite materials,<sup>13–15</sup> and metal oxides<sup>16</sup> are employed as the battery-type negative electrode material. In 2001, Amatucci *et al.*<sup>16,17</sup> firstly developed a hybrid device by using AC as a positive electrode material and nanostructured LTO as a negative electrode material, and the energy density of the packaged device reached in excess of 20 W h kg<sup>-1</sup> for the first time, nearly three times that of a conventional supercapacitor. Following this work, subsequent studies of hybrid supercapacitors based on the LTO negative electrode were also reported.<sup>12,14</sup> Regarding these studies, it should be noted that the voltage plateau of LTO-based materials is around 1.5 V *vs.* Li/Li<sup>+</sup>, thus the hybrid supercapacitor could be only charged and discharged under 3.2 V, leading to under-optimized utilization of AC positive material and thus a limited energy density. Besides, conventional LTO has the biggest problem of low power characteristic due to its inherent poor Li<sup>+</sup> diffusion coefficient<sup>18</sup> and poor electronic conductivity, thus greatly inhibiting the rate performance in the hybrid device. In another work, Béguin *et al.*<sup>13</sup> have designed a HSC using graphite as negative electrode material and AC as positive electrode for extending the operating voltage to 4.5 V, since graphite materials can be intercalated by Li<sup>+</sup> at more negative potentials (~0.1 V *vs.* Li/Li<sup>+</sup>),<sup>15</sup> thus the energy density could increase to 103.8 W h kg<sup>-1</sup>. Although much improved energy density can be achieved, the poor power capability of graphite materials would also greatly restrict the

power density of HSC. Furthermore, both of the two materials have low theoretical capacity when used as negative electrode materials (175 mA h g<sup>-1</sup> for LTO and 372 mA h g<sup>-1</sup> for graphite, respectively), which would also limit the energy density of HSC.

Metal oxides, such as SnO<sub>2</sub>,<sup>19,20</sup> Co<sub>3</sub>O<sub>4</sub>,<sup>21,22</sup> and Fe<sub>3</sub>O<sub>4</sub> (ref. 23–25) are also considered to be good candidates as negative electrode materials in HSC due to their large theoretical capacity (500–1000 mA h g<sup>-1</sup>) and relatively low voltage plateau (~0.8 V), which may dramatically improve the energy density for HSCs compared to LTO and graphite materials. Among these metal oxides, Fe<sub>3</sub>O<sub>4</sub> is attracting great attention for its advantages of high theoretical capacity (924 mA h g<sup>-1</sup>),<sup>26</sup> low cost, eco-friendliness and natural abundance. Nevertheless, to the best of our knowledge, there were rare reports on Li-ion type hybrid supercapacitor with a AC//metal oxide configuration,<sup>16</sup> probably because of the poor rate performance and cycle stability of metal oxides, which mainly result from severe aggregation and dramatic volume expansion after Li<sup>+</sup> insertion. Hence, to optimize the performance of HSC, the modification of Fe<sub>3</sub>O<sub>4</sub> materials has become a crucial issue. Graphene, with high specific surface area (SSA) and excellent conductivity,<sup>27</sup> is an ideal electrode material for energy storage devices.<sup>28,29</sup> Moreover, its two-dimensional structure makes it very suitable to fabricate composites with other electrochemical-active materials (such as CNTs,<sup>29–31</sup> metal oxides,<sup>32,33</sup> and polymers<sup>34,35</sup>) to enhance the whole electrochemical performance.

Herein, we successfully designed a hybrid supercapacitor using graphene-enhanced negative and positive electrode materials to both improve the energy and power density performance. A well-structured Fe<sub>3</sub>O<sub>4</sub> nanoparticle/graphene (Fe<sub>3</sub>O<sub>4</sub>/G) composite was prepared as the negative electrode material by a facile approach including solvothermal reaction and an easy heat treatment. The as-prepared Fe<sub>3</sub>O<sub>4</sub>/G exhibits high reversible specific capacity exceeding 1000 mA h g<sup>-1</sup> at the current density of 90 mA g<sup>-1</sup>, as well as excellent rate performance and cycle stability, which would benefit greatly to improve energy density for the hybrid device. Meanwhile, a graphene-based three dimensional porous carbon material (3DGraphene) with high SSA (~3355 m<sup>2</sup> g<sup>-1</sup>) and good conductivity was used as a positive electrode material to enhance electrochemical performance compared to commercial AC. Thereby, by employing these two graphene-enhanced materials, the Fe<sub>3</sub>O<sub>4</sub>/G//3DGraphene hybrid supercapacitor was fabricated with an improved ultrahigh energy density of 147 W h kg<sup>-1</sup> (power density of 150 W kg<sup>-1</sup>), which also remains of 86 W h kg<sup>-1</sup> even at high power density of 2587 W kg<sup>-1</sup>, so far the highest value of the reported hybrid supercapacitors.

## Experimental

### Synthesis of Fe<sub>3</sub>O<sub>4</sub>/G nanocomposite

The Fe<sub>3</sub>O<sub>4</sub>/graphene (Fe<sub>3</sub>O<sub>4</sub>/G) nanocomposite was prepared by an *in situ* solvothermal reaction using graphite oxide (GO) as the precursor. Typically, GO was prepared using modified Hummers method from flake graphite.<sup>36,37</sup> For synthesizing the optimized Fe<sub>3</sub>O<sub>4</sub>/G composite, ferric chloride (FeCl<sub>3</sub>·6H<sub>2</sub>O, 1.35 g, 5 mmol) and urea (0.6 g, 10 mmol) were added into

ethylene glycol (15 mL) and stirred for several minutes until an orange transparent solution was obtained. The solution was mixed with GO aqueous solution (30 mg, 60 mL distilled water) for 2 h and then transferred into a 100 mL Teflon-lined stainless steel autoclave. The sealed autoclave was heated up to 180 °C and maintained for 12 h. After the autoclave was naturally cooled to room temperature, the resulting precipitate was filtered and washed repeatedly with distilled water and dried in vacuum at 120 °C for 24 h. Finally the sample was heat-treated at 600 °C with a heating rate of 5 °C min<sup>-1</sup> and held for 4 h under argon atmosphere, and Fe<sub>3</sub>O<sub>4</sub>/G nanocomposite was obtained. According to thermogravimetric (TG) analysis (see Fig. S1 in the ESI†), the weight percentage of graphene content is 3.3 wt% in the Fe<sub>3</sub>O<sub>4</sub>/G composite. Bare Fe<sub>3</sub>O<sub>4</sub> and bare reduced graphene oxide (RGO) were synthesized by the same synthetic procedure as control materials.

### Synthesis of 3DGraphene

Briefly, homogeneous graphene oxide (5 mg mL<sup>-1</sup>) and sucrose (250 mg mL<sup>-1</sup>) aqueous solutions were mixed in different mass ratios of GO : sucrose (1 : 32, 24, 16, 8) and stirred for 4 h. Then the mixture was transferred to a sealed 100 mL Teflon-lined autoclave, heated up to 200 °C and maintained at this temperature for 12 h. The resulting solid product was then filtered, washed with distilled water and finally dried in vacuum at 120 °C for 24 h. The intermediate product was mixed with 4 × KOH, then placed in a horizontal tube furnace and heated from room temperature to 800 °C for 1 h at 5 °C min<sup>-1</sup> under an inert argon gas flow. After cooling down to the room temperature, the product was thoroughly washed with 0.1 M HCl, then washed with distilled water until the pH = 7 and finally dried in vacuum at 120 °C for 24 h. The obtained final products were defined as 3DGraphene which stands for porous graphene-based carbon material, as the products consist of mainly single-layered graphene sheets, of a few nanometers in size which are chemically bonded together as a whole bulk material (see Results and discussion below). Based on the results of surface area and conductivity data, the product with the optimized ratio of 1 : 24 of GO : sucrose was selected to be used as the EDLC electrode material for the hybrid supercapacitor device studies. The product synthesized by pure sucrose (denoted as SUAC) was also synthesized by the same synthetic procedure as comparison.

### Characterization

Scanning Electron Microscopy (SEM) was conducted using LEO 1530 VP field emission scanning electron microscope with acceleration voltage of 10 kV. Transmission electron microscopy (TEM) was carried out on a JEOL TEM-2100 electron microscope operated at 200 kV. Powder X-ray diffraction (XRD) measurements were performed on a Rigaku D/Max-2500 diffractometer with Cu K $\alpha$  radiation. Raman spectra were examined with a LabRAM HR Raman spectrometer using laser excitation at 514.5 nm. X-Ray photoelectron spectroscopy (XPS) was carried out using AXIS HIS 165 spectrometer (Kratos Analytical) with a monochromatized Al K $\alpha$  X-ray source (1486.71 eV photons). Thermogravimetric (TG) analysis (Netzsch-STA 449C) was

measured from 20 to 800 °C at a heating rate of 10 °C min<sup>-1</sup> in air. Nitrogen adsorption-desorption analysis was conducted at 77 K on a Micromeritics ASAP 2020 apparatus. The surface area was calculated by the BET method based on adsorption data in the relative pressure ( $P/P_0$ ) range of 0.05 to 0.3. The total pore volume was measured from the amount of nitrogen adsorbed at a relative pressure ( $P/P_0$ ) of 0.99. The pore size distribution (PSD) was analyzed using a NL-DFT method with a slit pore model from the nitrogen adsorption data. The electrical conductivity of positive electrode material 3DGraphene was tested by the following method. Typically, 3DGraphene was mixed with 1 wt% polytetrafluoroethylene (PTFE, solid powder, Dupont) as a binder, and homogenized in an agate mortar. Then it was rolled into 80–100  $\mu$ m thickness sheets and pressed by 20 MPa and finally cut into 3 × 1 cm<sup>2</sup> sheets. Then it was coated with silver conductive adhesives on both sides and tested using a multimeter. The conductivity of the film was calculated using the formula

$$\lambda = \frac{L}{R_x W d} \quad (1)$$

where  $\lambda$  is the electrical conductivity of sample,  $L$ ,  $W$ ,  $d$  is the length, width and thickness of the sheet respectively, and  $R_x$  is the resistance of the sheet tested by the multimeter.

### Fabrication of half cell and hybrid device

All the supercapacitor devices studied for the material performance in this work were fabricated using the industry standard method, and evaluated using the two-electrode industry level device following the method recommended best for industry practice<sup>38,39</sup> to get reliable performance data as much as possible. For fabrication of Fe<sub>3</sub>O<sub>4</sub>/G composite electrode, 85 wt% of active material Fe<sub>3</sub>O<sub>4</sub>/G, 10 wt% of acetylene black as the conducting filler, and 5 wt% of polyvinylidene fluoride (PVDF) in *N*-methyl-2-pyrrolidone (NMP) were well mixed and then coated onto 10  $\mu$ m thick copper foil which served as a current collector. After heating at 150 °C for 1 h, the sheet was pressed and punched into 1 cm diameter electrodes with loading mass of  $\sim$ 1.5 mg. For the cathode material 3DGraphene, a slightly different procedure was used. The 3DGraphene powder (tap density of  $\sim$ 0.4 g cm<sup>-3</sup>) was mixed directly with 10% polytetrafluoroethylene (PTFE), rolled into thin sheets, then punched into 1 cm diameter electrodes and hot pressed onto aluminum foil with conducting carbon coating. Half cells were firstly assembled for measuring the performance of each Fe<sub>3</sub>O<sub>4</sub>/G anode and 3DGraphene cathode separately. Both anode and cathode was tested using coin-type cells, where lithium metal foil was used as the counter and reference electrode, and 1 M LiPF<sub>6</sub> dissolved in 1 : 1 : 1 (v/v/v) mixture of ethylene carbonate/diethyl carbonate/dimethyl carbonate (EC/DEC/DMC) was employed as the electrolyte. Hybrid supercapacitors were also assembled in coin cells with pre-activated Fe<sub>3</sub>O<sub>4</sub>/G anode (charged-discharged for several cycles at low current density) and 3DGraphene cathode in the same electrolyte, and the optimized mass ratio of cathode/anode was 4.5 : 1.

## Electrochemical measurements

All the electrochemical tests were carried out at room temperature. Cyclic voltammetry (CV) and electrical impedance spectroscopy (EIS) studies were performed using Autolab (Metrohm). Galvanostatic charge–discharge measurements of half cells, symmetric supercapacitors and hybrid devices were carried out galvanostatically at various current densities with voltage windows specific to the materials using a battery test system (LAND CT2001A model, Wuhan LAND Electronics. Ltd.). The specific capacitance  $C_s$  ( $F\ g^{-1}$ ) of 3DGraphene in the symmetric supercapacitor was calculated according to the formation

$$C_s = \frac{4I}{m\ dV/dt} \quad (2)$$

where  $I$  is the constant current (A),  $m$  (g) is the total mass of two electrodes, and  $dV/dt$  ( $V\ s^{-1}$ ) is the slope obtained by fitting a straight line to the discharge curve.

The energy density values  $E$  ( $W\ h\ kg^{-1}$ ) of symmetric supercapacitors and hybrid supercapacitors were calculated by numerically integrating the  $Q$ - $V$  graph (or  $t$ - $V$  graph, as the current density  $I$  is a constant value) area during the discharge process,<sup>40</sup> using the formula (followed by unit conversion to  $W\ h\ kg^{-1}$ )

$$E = \int_{t_1}^{t_2} IV\ dt \quad (3)$$

where  $I$  is the constant current density ( $A\ g^{-1}$ ),  $V$  (V) is the voltage, and  $t_1$ ,  $t_2$  is the start time and end time in the discharge process, respectively.

The power density values  $P$  ( $W\ kg^{-1}$ ) of symmetric supercapacitors and hybrid supercapacitors were calculated according to

$$P = E/\Delta t \quad (4)$$

where  $\Delta t$  is the discharge time.

## Results and discussion

### Characterization of $Fe_3O_4/G$ nanocomposite as the negative electrode material

The  $Fe_3O_4/G$  nanocomposite was prepared by a simple *in situ* solvothermal method using graphite oxide (GO) and  $FeCl_3$  as the precursor, and followed by the annealing process  $600\ ^\circ C$  (Scheme 1). The composites with different ratios of graphene and  $Fe_3O_4$  were synthesized. The optimized product with only 3.3 wt% of graphene (determined by the thermogravimetric analysis, Fig. S1†) was selected and discussed below. Fig. 1 shows the structure characterization of as-prepared  $Fe_3O_4/G$  composite. Fig. 1a shows the X-ray diffraction (XRD) profile of  $Fe_3O_4/G$  with commercial  $Fe_3O_4$  as contrast, which reveals that all the peaks of the  $Fe_3O_4/G$  composite can be assigned to  $Fe_3O_4$  (JCPDS no. 65-3107). Furthermore, no obvious peaks in the range of  $24$ – $28^\circ$  corresponding to graphene stacking are observed, which can be ascribed to the very little content of graphene ( $\sim 3.3$  wt%) and the disordered distribution of

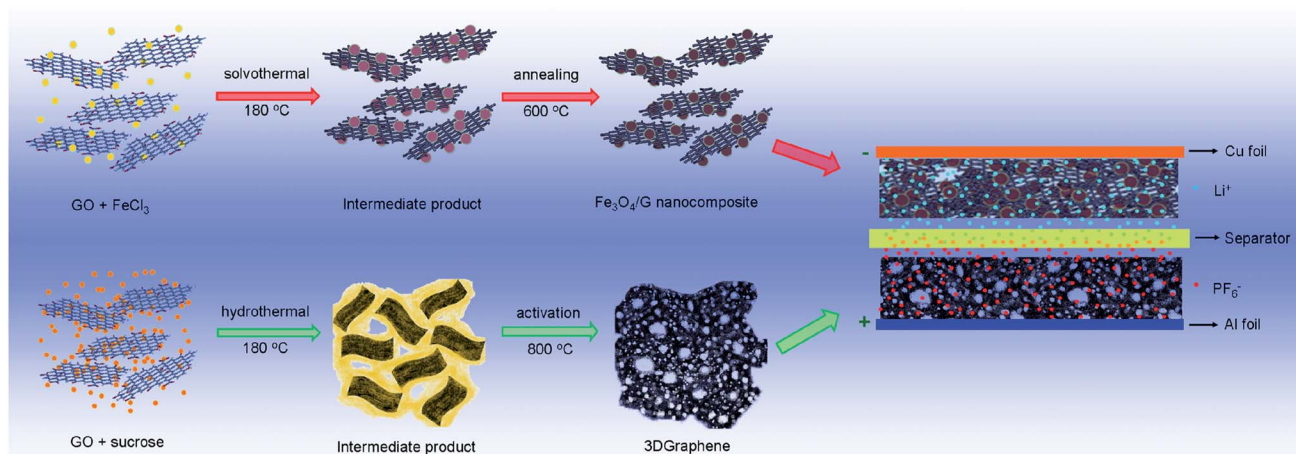
graphene sheets in the  $Fe_3O_4/G$  composite<sup>26</sup> (confirmed by the SEM images in the following). Raman spectra of  $Fe_3O_4/G$  composite, commercial  $Fe_3O_4$  particles and graphene are also shown in Fig. 1b. The Raman spectrum of the  $Fe_3O_4/G$  composite exhibits typical peaks of  $Fe_3O_4$  ( $302$ ,  $540$ , and  $670\ cm^{-1}$ , corresponding to the  $E_g$ ,  $T_{2g}$ , and  $A_{1g}$  vibration modes respectively)<sup>32</sup> and characteristic peaks of graphene (with the D-band and G-band at around  $1355$  and  $1597\ cm^{-1}$ , respectively).<sup>41</sup>

The morphology of the  $Fe_3O_4/G$  composite was characterized by scanning electron microscopy (SEM) and transmission electron microscopy (TEM). The SEM images (Fig. 1c and d) show that the small  $Fe_3O_4$  particles with sizes of  $100$ – $200$  nm are distributed in graphene nanosheets. The TEM image (Fig. 1e) further indicates that the two-dimensional graphene sheets are well decorated by a large quantity of  $Fe_3O_4$  nanoparticles and both the outline of graphene and  $Fe_3O_4$  nanoparticles can be clearly observed. The HR-TEM image in Fig. 1f shows the interfacial structure between  $Fe_3O_4$  nanoparticle and graphene, and the crystal lattice fringes with a  $d$ -spacing of  $0.25$  nm comes from the (311) plane of  $Fe_3O_4$ . These results are consistent with XRD and Raman results. The homogeneously distributed graphene sheets among the  $Fe_3O_4$  nanoparticles not only act as a good conductive network throughout the composite but also prevent  $Fe_3O_4$  nanoparticles from agglomeration (Fig. S3†), which is the key reason for the poor cycling performance of the conventional  $Fe_3O_4$  based devices. Moreover, from the result of nitrogen isothermal adsorption measurement (Fig. S4†), it is clearly seen that with the introduction of a few percents of graphene, the specific surface area (SSA) of the products is increased from  $4\ m^2\ g^{-1}$  to  $47\ m^2\ g^{-1}$  (calculated by the BET method in relative pressure range from  $0.05$  to  $0.3$ ), which can greatly enhance electrode–electrolyte interface and is beneficial for electrolyte access. Therefore, the small  $Fe_3O_4$  particle size on graphene, along with the improved conductivity and electrolyte accessibility would indicate an enhancement of the electrochemical performance in aspect of the rate performance and cycle stability.

The electrochemical performances of  $Fe_3O_4/G$  nanocomposite were investigated using half cells vs.  $Li/Li^+$  in the potential range  $0.01$ – $3$  V, as shown in Fig. 2. Fig. 2a shows the cyclic voltammetry (CV) curves of  $Fe_3O_4/G$  electrode in the first three discharge–charge cycles at a scan rate of  $0.5\ mV\ s^{-1}$ . In the first cycle, two obvious peaks are observed at about  $0.76$  V and  $0.48$  V in the cathodic polarization process, corresponding to the reaction  $Fe_3O_4 + 8Li^+ + 8e^- \rightarrow 3Fe^0 + 4Li_2O$ .<sup>42</sup> Meanwhile, a peak was recorded at about  $1.89$  V during the anodic process, which should be attributed to the oxidation of  $Fe^0$  to  $Fe_3O_4$ .<sup>43,44</sup> After the first cycle, both cathodic and anodic peaks are shifted, which is ascribed to polarization of the electrode in the first cycle.<sup>45</sup> Moreover, the CV curves of the  $Fe_3O_4/G$  nanocomposite in the subsequent two cycles almost overlap, revealing a good reversibility.

The galvanostatic charge–discharge curves of  $Fe_3O_4/G$  nanocomposite (Fig. 2b) is obtained at a current density of  $90\ mA\ g^{-1}$  (corresponding to  $\sim 0.1$  C rate) and the cell exhibits a first cycle reversible specific capacity as high as  $1089\ mA\ h\ g^{-1}$  based on the total mass of electrode active material, which is





**Scheme 1** Schematic show of the synthesis of the negative electrode material  $\text{Fe}_3\text{O}_4/\text{G}$  nanocomposite and the positive electrode material 3D Graphene, together for the configuration of a Li-ion containing organic hybrid supercapacitor.

higher than the theoretical capacity for  $\text{Fe}_3\text{O}_4$ -based anodes as well as the specific capacity of as-prepared  $\text{Fe}_3\text{O}_4$  ( $723 \text{ mA h g}^{-1}$ ) and as-prepared graphene ( $312 \text{ mA h g}^{-1}$ ) (Fig. 2c). The irreversible capacity loss in the first cycle can be attributed to the formation of solid electrolyte interface (SEI) film.<sup>43,46</sup> Moreover, the Coulombic efficiency in the first cycle can reach up to 84.1%, which is much higher than that of the bare as-prepared  $\text{Fe}_3\text{O}_4$  (57.3%), indicating a high reversible capacity of the composite. Additionally, the specific capacity of the  $\text{Fe}_3\text{O}_4/\text{G}$  composite decreases very slowly when increasing charge-discharge current densities, illustrating an excellent rate performance (Fig. 2c). For example, when the current density

increases to  $2700 \text{ mA g}^{-1}$  ( $\sim 3\text{C}$  rate), the specific capacity of the  $\text{Fe}_3\text{O}_4/\text{G}$  composite still remains  $704 \text{ mA h g}^{-1}$ , 65% of the initial capacity, much larger than those previous reports.<sup>26,32</sup> In contrast, the capacity of the as-prepared  $\text{Fe}_3\text{O}_4$  fades dramatically to only 5% of the initial capacity at the same high current density. Furthermore, the  $\text{Fe}_3\text{O}_4/\text{G}$  composite also exhibits good cycle stability as shown in Fig. 2d. After 100 charge-discharge cycles at a high current density of  $2700 \text{ mA g}^{-1}$ , the specific capacity still keeps 90% retention. Besides, the Coulombic efficiency is nearly 100% in every cycle. These results clearly demonstrate an important role of the well-organized interleaved structure of the  $\text{Fe}_3\text{O}_4/\text{G}$  composite in improving the

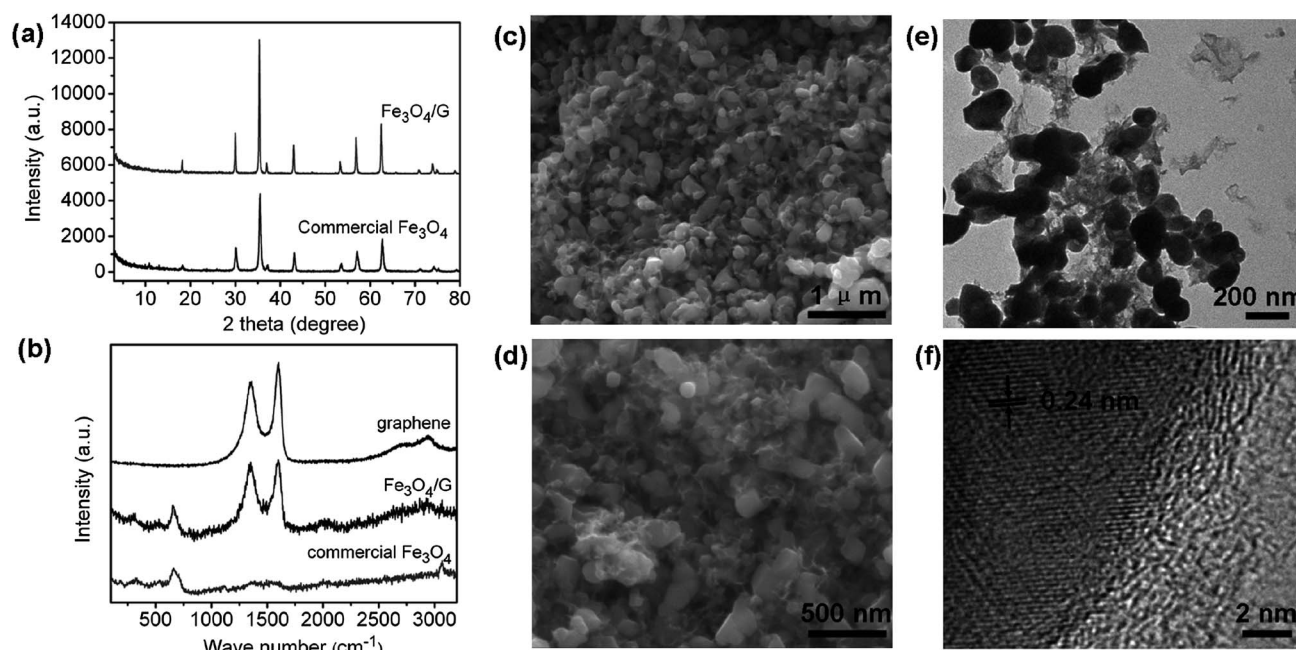


**Fig. 1** (a) XRD patterns of as-prepared  $\text{Fe}_3\text{O}_4/\text{G}$  composite and commercial  $\text{Fe}_3\text{O}_4$  as comparison. (b) Raman spectra of  $\text{Fe}_3\text{O}_4/\text{G}$  composite, commercial  $\text{Fe}_3\text{O}_4$  and graphene. (c and d) SEM images of  $\text{Fe}_3\text{O}_4/\text{G}$  nanocomposite in different magnification. (e and f) TEM and HR-TEM images of  $\text{Fe}_3\text{O}_4/\text{G}$  nanocomposite. The particle size of  $\text{Fe}_3\text{O}_4$  is about 100–200 nm, and the graphene sheets are well decorated by a large quantity of  $\text{Fe}_3\text{O}_4$  nanoparticles.

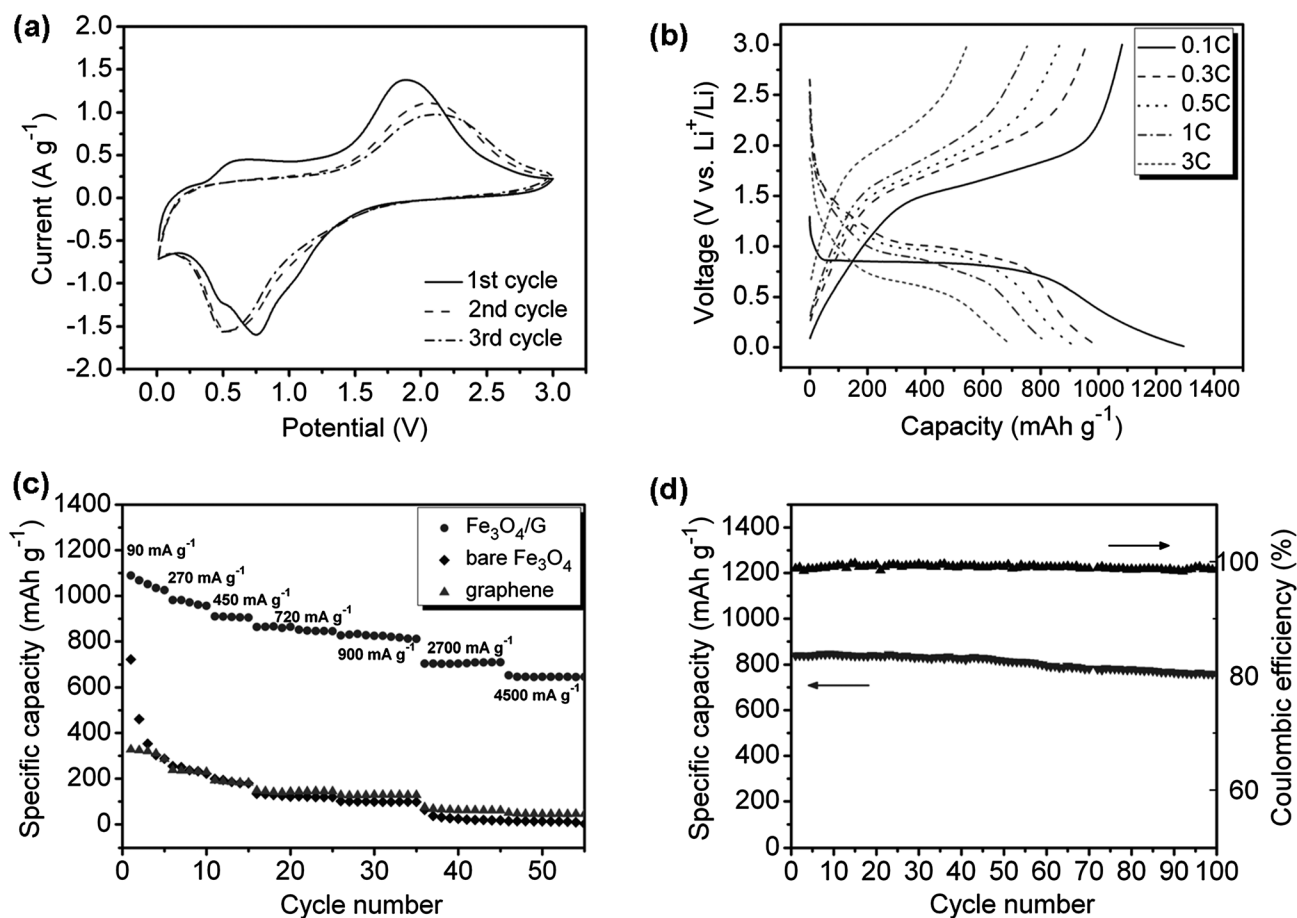


**Fig. 2** Electrochemical performances of  $\text{Fe}_3\text{O}_4/\text{G}$  based half cell (vs.  $\text{Li}/\text{Li}^+$ ) in the potential range of 0.01–3 V. (a) Cyclic voltammograms (CV) curves of  $\text{Fe}_3\text{O}_4/\text{G}$  in the first three discharge–charge cycles at  $0.5 \text{ mV s}^{-1}$ . (b) Charge–discharge curves of  $\text{Fe}_3\text{O}_4/\text{G}$  electrode at different current densities of 0.1–3 C (1 C =  $900 \text{ mA h g}^{-1}$ ). (c) Rate performance of  $\text{Fe}_3\text{O}_4/\text{G}$ , as-prepared  $\text{Fe}_3\text{O}_4$  and graphene at different current densities. (d) Cycle stability of  $\text{Fe}_3\text{O}_4/\text{G}$  at a current density of  $720 \text{ mA g}^{-1}$  for 100 cycles, with high Coulombic efficiency of nearly 100%.

electrochemical performance. The high reversible capacity, excellent rate performance and improved cycle stability can be attributed to following three critical features. First, graphene can act as a reaction template in  $\text{Fe}_3\text{O}_4$  particles formation, which would inhibit the agglomeration of the  $\text{Fe}_3\text{O}_4$  particles and control the size to nanometers, thus would improve utilization of  $\text{Fe}_3\text{O}_4$  and get a high reversible capacity. Second, the as-formed three-dimensional (3D) porous networks also create interconnected channels, favorable for fast  $\text{Li}^+$  transport and effective electron transport, contributing to an excellent rate performance. Third, the two-dimensional graphene nanosheets act as “elastic buffer” to alleviate the cracking of  $\text{Fe}_3\text{O}_4$  nanoparticles and inhibit the volume variations and agglomeration of pulverized  $\text{Fe}_3\text{O}_4$  during Li uptake release cycles, which is beneficial to cycle stability. Such extraordinary properties of  $\text{Fe}_3\text{O}_4/\text{G}$  make it a good candidate for hybrid supercapacitor with an improved energy density and power density.

#### Characterization of 3DGraphene as positive electrode material

Before fabricating a hybrid device, the positive electrode material 3DGraphene was also synthesized and characterized, as shown in

Fig. 3. The three dimensional graphene-based porous carbon material (3DGraphene) was derived from GO and sucrose as the precursor with the optimized ratio of 1 : 24, using the hydrothermal reaction and the following activation process (Scheme 1) described in the Experimental section. The microstructure of the as-prepared 3DGraphene was shown from the HRTEM images in Fig. 3a and b, which exhibit highly porous structures surrounded by highly curved carbon nanosheets. The highly defected (wrinkled and/or twisted) and porous structure indicates a fast ion transport channel for the supercapacitor application. Besides, the X-ray photoelectron spectroscopy (XPS) confirms that the carbon atoms mainly exist in the  $\text{sp}^2$  carbon form, which means the most stable six-membered ring form (Fig. S5a†). Moreover, the XRD profile (Fig. S5b†) displays a broad and weak (002) peak from  $15^\circ$  to  $25^\circ$ , demonstrating a much disordered and porous structure in the material. Meanwhile, the average graphene domains height ( $L_c$ ) can be approximately determined to be  $\sim 0.748 \text{ nm}$  (calculated by the Scherrer's equation<sup>47</sup>), thus the graphene domains are mainly composed of single-layered curved graphene sheets. Raman spectroscopy was also tested to estimate the size of the graphene domains, and the average domain size  $L_a$  of  $\sim 6.6 \text{ nm}$  was obtained by the equation<sup>48</sup>

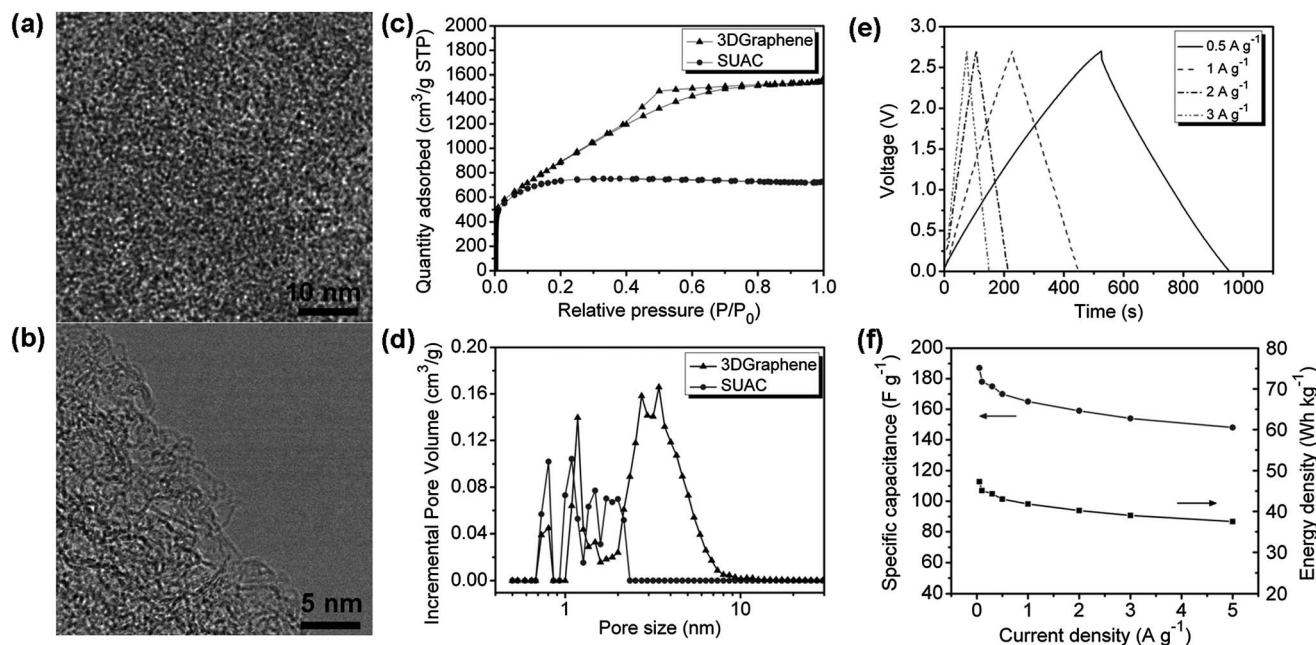


**Fig. 3** (a and b) High Resolution TEM (HRTEM) images of positive material 3DGraphene. (c)  $N_2$  adsorption–desorption isotherms of positive electrode material 3DGraphene and pure SUAC as contrast. (d) Pore size distribution of 3DGraphene and SUAC as contrast, calculated using a NLDFT model. (e) Galvanostatic charge–discharge curves of 3DGraphene-based supercapacitor at different current densities in the voltage range of 0–2.7 V. (f) Specific capacitances and energy densities of 3DGraphene-based supercapacitor at different densities. All these values were calculated based on the mass of single electrode activated material.

$L_a$  (nm) =  $(560/\lambda^4)(I_D/I_G)^{-1}$  (Fig. S5c†). All these data indicate that the materials consist of mainly curved single-layered graphene sheets in the size of a few nanometers, which structure may contribute to a high specific surface area of material.<sup>49</sup> Moreover, the 3DGraphene material achieves an ultrahigh SSA of  $3355 \text{ m}^2 \text{ g}^{-1}$  with mesoporosity according to the type IV characteristic sorption–desorption isotherm (Fig. 3c). Fig. 3d further reveals a well-controlled pore size distribution of primarily 2–6 nm width pores in 3DGraphene. On the contrary, the product SUAC derived from bare sucrose without graphene only obtains relatively low SSA of  $2536 \text{ m}^2 \text{ g}^{-1}$  with a mainly micropore structure. Besides, the conductivity of 3DGraphene ( $\sim 77 \text{ S m}^{-1}$ ) is also higher than SUAC ( $\sim 51 \text{ S m}^{-1}$ ). All these results indicates that the introduction of graphene (only 4 wt%) plays a great important role in building the 3D porous structure of the product as well as increasing the SSA and conductivity, which would result in a better electrochemical performance in the Li-ion based electrolyte.

For examining the EDLC performance of the 3DGraphene material, a symmetrical supercapacitor was assembled with two identical 3DGraphene electrodes with equal size and weight in  $\text{LiPF}_6$ -based organic electrolyte. Fig. 3e shows galvanostatic charge–discharge curves at different current densities. The curves are nearly straight lines, illustrating a standard capacitive behavior of EDLC-type supercapacitors.<sup>50</sup> As expected, the 3DGraphene-based supercapacitor exhibits both high specific capacitance/energy and excellent rate performance. As shown in Fig. 3f, the specific capacitance of 3DGraphene in the Li-ion electrolyte is in the range from 148 to  $187 \text{ F g}^{-1}$  at current densities of 5.0 to  $0.05 \text{ A g}^{-1}$  from 0–2.7 V, and the energy density could reached to  $37.5\text{--}47.3 \text{ Wh kg}^{-1}$  at the same ranged current densities. In contrast, the SUAC product shows lower

specific capacitance of  $126\text{--}141 \text{ F g}^{-1}$  and energy density of  $31.1\text{--}35.7 \text{ Wh kg}^{-1}$  under the similar condition (Fig. S6†).

### Hybrid supercapacitor based on $\text{Fe}_3\text{O}_4/\text{G}$ nanocomposite and 3DGraphene

As mentioned above, with high specific capacity, excellent rate performance and improved cycle stability, the as-prepared  $\text{Fe}_3\text{O}_4/\text{G}$  nanocomposite and 3DGraphene should be promising electrode materials for high-energy hybrid supercapacitor. In order to further investigate this potential superiority, we designed a hybrid supercapacitor in  $\text{LiPF}_6$ -containing organic electrolyte, consisting of a negative electrode of  $\text{Fe}_3\text{O}_4/\text{G}$  nanocomposite and a positive electrode of 3DGraphene (see Scheme 1). During the charge process,  $\text{PF}_6^-$  ions are absorbed in the porous structure of 3DGraphene (positive electrode), while Li ions from electrolyte are intercalated into the  $\text{Fe}_3\text{O}_4/\text{G}$  nanocomposite (negative electrode). Discharge process is in reverse of the charge process.

In order to obtain high energy density of such a hybrid device, the working potential range and the mass ratio of the electrodes need to be optimized to make full use of the performance of both electrode materials. As shown in Fig. 2b, the plots demonstrate a slow decrease of curve-shaped slope in the potential region from 1.5 to 0.0 V (vs.  $\text{Li}/\text{Li}^+$ ) because of a plateau region at the negative electrode  $\text{Fe}_3\text{O}_4/\text{G}$ . Meanwhile, the positive electrode 3DGraphene shows a linear curve (Fig. S7†) in the potential region from 2.5 to 4.0 V (vs.  $\text{Li}/\text{Li}^+$ ). Based on these data, the performance of  $\text{Fe}_3\text{O}_4/\text{G}/\text{PG}$  hybrid supercapacitors was measured in the voltage window of 1.0–4.0 V. On the other hand, according to the equation  $Q_+ = Q_-$



( $m_+q_+ = m_-q_-$ , where  $Q$  and  $q$  stands for the capacity and specific capacity, respectively, and  $m$  is the mass of activated electrode material), the respective masses of the two electrodes must be adjusted to equalize the capacity, because the specific capacity of the  $\text{Fe}_3\text{O}_4/\text{G}$  negative electrode material is different from that of the 3DGraphene positive electrode material. As the specific capacity of  $\text{Fe}_3\text{O}_4/\text{G}$  negative electrode is much higher than that of 3DGraphene positive electrode, the performance of hybrid devices was measured in the different mass ratios of 3DGraphene:  $\text{Fe}_3\text{O}_4/\text{G}$  from 3.0 to 6.0, which is shown in Fig. S8a.† At the mass ratio of 3DGraphene:  $\text{Fe}_3\text{O}_4/\text{G} = 4.5 : 1$ , the hybrid cell achieves the highest energy density of  $147 \text{ W h kg}^{-1}$  under the same power density ( $\sim 150 \text{ W kg}^{-1}$ ), and the tendency remains almost the same with increasing the charging–discharging rate (see Fig. S8b)†, thus the best mass ratio of 4.5 : 1 is selected in the work.

The electrochemical performance of  $\text{Fe}_3\text{O}_4/\text{G}/3\text{DGraphene}$  hybrid supercapacitor with the optimal mass ratio of 4.5 : 1 in the potential range of 1.0–4.0 V is shown in Fig. 4. Fig. 4a shows the CV curves in various scan rates. Different from the symmetric supercapacitor, the  $\text{Fe}_3\text{O}_4/\text{G}/3\text{DGraphene}$  hybrid supercapacitor exhibits a gradual deviation from the ideal rectangular shape with increasing scan rate, which is owing to

the synergistic effect of two different energy-storage mechanisms. Fig. 4b shows galvanostatic charge–discharge curves at different current densities (based on the negative electrode). It is noted that the slopes of the curves are not strictly linear especially at low current densities, indicating that the hybrid supercapacitor exhibited charge–discharge performances of the combination of a supercapacitor and a battery. In the charge process, the hybrid device potential plot shows a slow decrease in the curve-shaped slope because of a plateau region at the negative electrode from the  $\text{Li}^+$  lithiation/delithiation reaction around 0.8–1.5 V vs.  $\text{Li}/\text{Li}^+$ . Then the linear slope of the hybrid device potential profile indicates a linear plot with a higher slope, which is due to the end of the plateau region of the negative electrode below 0.8 V vs.  $\text{Li}/\text{Li}^+$ . The discharge process is reversed of the charge process. The  $\text{Fe}_3\text{O}_4/\text{G}/3\text{DGraphene}$  hybrid supercapacitor also exhibits a passable cycle stability (Fig. 4c) with the capacity retention of 70% after 1000 cycling numbers at a high current density of  $2 \text{ A g}^{-1}$ , with high Coulombic efficiency of  $\sim 100\%$  during cycles.

The Ragone plot (energy density vs. power density) of the  $\text{Fe}_3\text{O}_4/\text{G}/3\text{DGraphene}$  hybrid supercapacitor and 3DGraphene//3DGraphene symmetric supercapacitor as contrast are shown in Fig. 4d. The energy density and power density are calculated

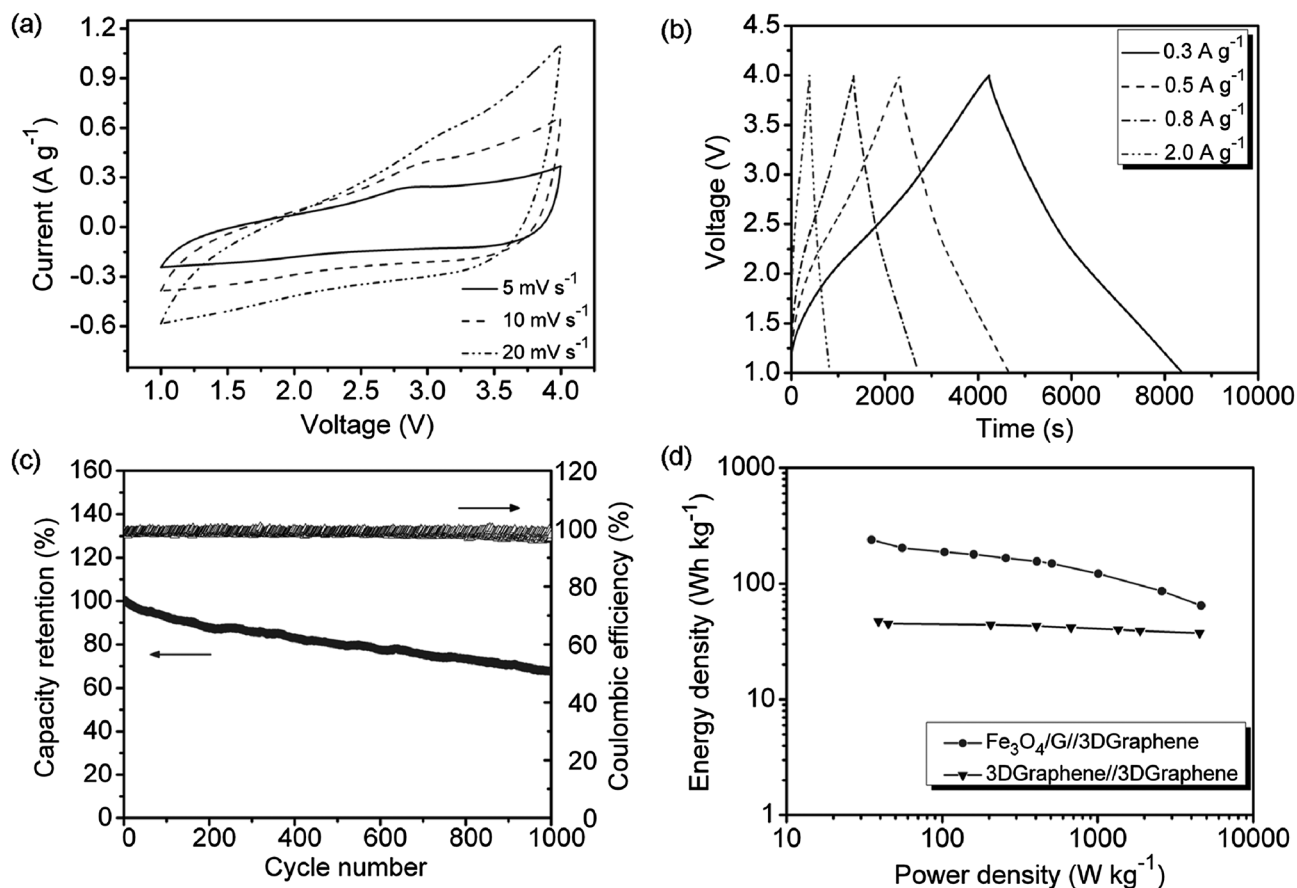


**Fig. 4** Electrochemical performance of  $\text{Fe}_3\text{O}_4/\text{G}/3\text{DGraphene}$  hybrid supercapacitor at the optimal mass ratio of  $m_{\text{positive}}/m_{\text{negative}} = 4.5 : 1$ . (a) CV curves of  $\text{Fe}_3\text{O}_4/\text{G}/3\text{DGraphene}$  hybrid supercapacitor in various scan rates of 5, 10, 20  $\text{mV s}^{-1}$ . (b) Galvanostatic charge–discharge curves at different current densities of 0.3–2.0  $\text{A g}^{-1}$ . (c) Cycle stability of  $\text{Fe}_3\text{O}_4/\text{G}/3\text{DGraphene}$  hybrid supercapacitor for 1000 cycles at a current density of 2  $\text{A g}^{-1}$ . (d) Ragone plots of the  $\text{Fe}_3\text{O}_4/\text{G}/3\text{DGraphene}$  hybrid supercapacitor and 3DGraphene//3DGraphene symmetric supercapacitor as contrast at various charge–discharge rates.



based on the total mass of both electrodes. It can be clearly seen that both energy density and power density of the  $\text{Fe}_3\text{O}_4/\text{G}/3\text{DGraphene}$  hybrid supercapacitor are much higher than the  $3\text{DGraphene}/3\text{DGraphene}$  symmetric supercapacitor for comparison. At a low power density of  $55 \text{ W kg}^{-1}$ , the hybrid capacitor can achieve the ultrahigh energy density of  $204 \text{ W h kg}^{-1}$ , while the symmetric supercapacitor gets only  $45 \text{ W h kg}^{-1}$ . Meanwhile, when the power density increases to  $\sim 1000 \text{ W kg}^{-1}$ , the energy density of the hybrid capacitor still keeps higher ( $122 \text{ W h kg}^{-1}$ ) than the symmetric capacitor ( $40 \text{ W h kg}^{-1}$ ), exhibiting prominent rate performance.

Furthermore, compared with the performance of other reported various hybrid supercapacitors, such as graphite//AC system,<sup>7</sup> LTO-AC//AC system,<sup>5</sup>  $\text{H}_2\text{Ti}_6\text{O}_{13}$ //CMK-3 system,<sup>51</sup>  $\text{TiO}_2\text{-B}/\text{CNT}$  system,<sup>52</sup> AC// $\text{V}_2\text{O}_5$  system,<sup>53</sup> it can be concluded that the  $\text{Fe}_3\text{O}_4/\text{G}/3\text{DGraphene}$  hybrid supercapacitor reaches the highest energy density with an improved power density, which is summarized in Fig. 5a. It is also worthy to note that for a packaged cell, the  $\text{Fe}_3\text{O}_4/\text{G}/3\text{DGraphene}$  hybrid device has much higher energy density than the commercial electrochemical capacitors and can be even compared with Ni-metal hydride and commercial lithium-ion batteries (LIBs), while the power density

can also retain an appropriate value, which means a faster charge-discharge rate than commercial LIBs (Fig. 5b). For instance, the gravimetric energy density based on the packaged  $\text{Fe}_3\text{O}_4/\text{G}/3\text{DGraphene}$  hybrid cell can be expected to be close to  $30 \text{ W h kg}^{-1}$  at a packaged power density of  $1000 \text{ W kg}^{-1}$  (while the volume power density is about  $16 \text{ W h L}^{-1}$  at a packaged power density of  $540 \text{ W L}^{-1}$ ), as the active electrode materials are about 35–40% of the total packaged mass.<sup>5</sup> These values demonstrate synergistic effects of LIBs (about  $10 \text{ W h kg}^{-1}$  at  $1000 \text{ W kg}^{-1}$ ) and EDLCs (about  $5 \text{ W h kg}^{-1}$  at  $5000 \text{ W kg}^{-1}$ ).<sup>54</sup>

## Conclusions

In summary, a supercapacitor–battery hybrid energy storage device, combining  $\text{Fe}_3\text{O}_4/\text{G}$  nanocomposite based negative electrode and 3DGraphene (3D porous graphene-based carbon material) based positive electrode, is successfully designed and studied for the first time. The  $\text{Fe}_3\text{O}_4/\text{G}/3\text{DGraphene}$  hybrid system exhibits energy densities of  $204\text{--}65 \text{ W h kg}^{-1}$  over the power densities from  $55$  to  $4600 \text{ W kg}^{-1}$ , which are the highest values for hybrid supercapacitors that ever reported before. The high-performance of the hybrid system is attributed to both the graphene-enhanced high-performance electrode materials. As an improved negative electrode, the as-prepared  $\text{Fe}_3\text{O}_4/\text{G}$  achieves both high specific capacity of  $>1000 \text{ mA h g}^{-1}$  at  $90 \text{ mA g}^{-1}$  and good rate performance of  $704 \text{ mA h g}^{-1}$  at  $2700 \text{ mA g}^{-1}$  in  $\text{LiPF}_6$  containing organic electrolyte with good cycle stability; meanwhile, the positive electrode material 3DGraphene also exhibits high EDLC specific capacitance as well as rate capability. These combined features make the hybrid supercapacitor exhibit a remarkable energy density much higher than the commercial supercapacitors, and can even compare with commercial lithium-ion batteries with improved power density.

## Acknowledgements

The authors gratefully acknowledge financial support from MoST (Grants 2012CB933401 and 2011DFB50300), NSFC (Grants 50933003 and 51273093).

## Notes and references

- 1 D. Linden and T. B. Reddy, *Handbook of Batteries*, McGraw-Hill, New York, 1995.
- 2 Y. Zhai, Y. Dou, D. Zhao, P. F. Fulvio, R. T. Mayes and S. Dai, *Adv. Mater.*, 2011, **23**, 4828.
- 3 B. E. Conway, *Electrochemical Supercapacitors: Scientific Fundamentals and Technological Applications*, Plenum, New York, 1999.
- 4 I. Plitz, A. D. Pasquier, F. Badway, J. Gural, N. Pereira, A. Gmitter and G. G. Amatucci, *Appl. Phys. A: Mater. Sci. Process.*, 2006, **82**, 615.
- 5 H. S. Choi, J. H. Im, T. Kim, J. H. Park and C. R. Park, *J. Mater. Chem.*, 2012, **22**, 16986.
- 6 S. R. Sivakkumar and A. G. Pandolfo, *Electrochim. Acta*, 2012, **65**, 280.

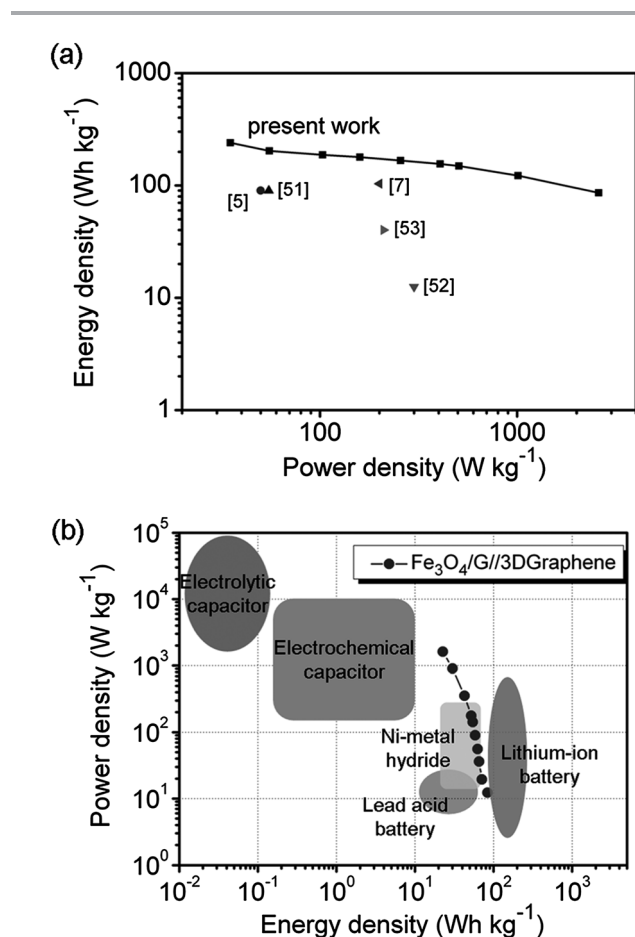


**Fig. 5** Ragone plots (energy density vs. power density) of  $\text{Fe}_3\text{O}_4/\text{G}/3\text{DGraphene}$  hybrid capacitor compared with (a) other reported hybrid supercapacitors (all based on total mass of both electrodes); (b) commercial electronic energy storage devices (all based on total mass of packaged device).

- 7 H. Wang, M. Yoshio, A. K. Thapa and H. Nakamura, *J. Power Sources*, 2007, **169**, 375.
- 8 H. Jiang, P. S. Lee and C. Li, *Energy Environ. Sci.*, 2013, **6**, 41.
- 9 J. Zhu, M. Chen, H. Qu, Z. Luo, S. Wu, H. A. Colorado, S. Wei and Z. Guo, *Energy Environ. Sci.*, 2013, **6**, 194.
- 10 L. Zhang, F. Zhang, X. Yang, G. K. Long, Y. P. Wu, T. F. Zhang, K. Leng, Y. Huang, Y. F. Ma, A. Yu and Y. S. Chen, *Sci. Rep.*, 2013, **3**, 408.
- 11 L. Zhang, F. Zhang, X. Yang, K. Leng, Y. Huang and Y. S. Chen, *Small*, 2013, DOI: 10.1002/sml.201202943.
- 12 J. Ni, L. Yang, H. Wang and L. Gao, *J. Solid State Electrochem.*, 2012, **16**, 2791.
- 13 V. Khomenko, E. P. Raymundo and F. Béguin, *J. Power Sources*, 2008, **177**, 643.
- 14 M. D. Stoller, S. Murali, N. Quarles, Y. Zhu, J. R. Potts, X. Zhu, H. W. Ha and R. S. Ruoff, *Phys. Chem. Chem. Phys.*, 2012, **14**, 3388.
- 15 S. R. Sivakkumar, J. Y. Nerkar and A. G. Pandolfo, *Electrochim. Acta*, 2010, **55**, 3330.
- 16 G. G. Amatucci, F. Badway, A. D. Pasquier and T. Zheng, *J. Electrochem. Soc.*, 2001, **148**, A930.
- 17 A. D. Pasquier, I. Plitz, J. Gural, S. Menocal and G. G. Amatucci, *J. Power Sources*, 2003, **113**, 62.
- 18 S. Takai, M. Kamata, S. Fujine, K. Yoneda, K. Kanda and T. Esaka, *Solid State Ionics*, 1999, **123**, 165.
- 19 X. W. Lou, J. S. Chen, P. Chen and L. A. Archer, *Chem. Mater.*, 2009, **21**, 2868.
- 20 P. Meduri, C. Pendyala, V. Kumar, G. U. Sumanasekera and M. K. Sunkara, *Nano Lett.*, 2009, **9**, 612.
- 21 N. Du, H. Zhang, B. D. Chen, J. B. Wu, X. Y. Ma, Z. H. Liu, Y. Q. Zhang, D. R. Yang, X. H. Huang and J. P. Tu, *Adv. Mater.*, 2007, **19**, 4505.
- 22 S. B. Yang, X. L. Feng, S. Ivanovici and K. Müllen, *Angew. Chem., Int. Ed.*, 2010, **49**, 8408.
- 23 S. Mitra, P. Poizot, A. Finke and J. M. Tarascon, *Adv. Funct. Mater.*, 2006, **16**, 2281.
- 24 Y. Piao, H. S. Kim, Y.-E. Sung and T. Hyeon, *Chem. Commun.*, 2010, **46**, 118.
- 25 S. Wang, J. Zhang and C. Chen, *J. Power Sources*, 2010, **195**, 5379.
- 26 P. Lian, X. Zhu, H. Xiang, Z. Li, W. Yang and H. Wang, *Electrochim. Acta*, 2010, **56**, 834.
- 27 S. Stankovich, D. A. Dikin, G. H. B. Dommett, K. M. Kohlhaas, E. J. Zimney, E. A. Stach, R. D. Piner, S. T. Nguyen and R. S. Ruoff, *Nature*, 2006, **442**, 282.
- 28 Y. Wang, Z. Q. Shi, Y. Huang, Y. F. Ma, C. Y. Wang, M. M. Chen and Y. S. Chen, *J. Phys. Chem. C*, 2009, **113**, 13103.
- 29 Y. P. Wu, T. F. Zhang, F. Zhang, Y. Wang, Y. F. Ma, Y. Huang, Y. Y. Liu and Y. S. Chen, *Nano Energy*, 2012, **1**, 820.
- 30 Y. Wang, Y. P. Wu, Y. Huang, F. Zhang, X. Yang, Y. F. Ma and Y. S. Chen, *J. Phys. Chem. C*, 2011, **115**, 23192.
- 31 N. Jha, P. Ramesh, E. Bekyarova, M. E. Itkis and R. C. Haddon, *Adv. Energy Mater.*, 2012, **2**, 438.
- 32 G. Zhou, D. W. Wang, F. Li, L. Zhang, N. Li, Z. S. Wu, L. Wen, G. Q. Lu and H. M. Cheng, *Chem. Mater.*, 2010, **22**, 5306.
- 33 Y. Su, S. Li, D. Wu, F. Zhang, H. Liang, P. Gao, C. Cheng and X. Feng, *ACS Nano*, 2012, **6**, 8349.
- 34 K. Zhang, L. L. Zhang, X. S. Zhao and J. Wu, *Chem. Mater.*, 2010, **22**, 1392.
- 35 A. K. Sarker and J. D. Hong, *Langmuir*, 2012, **28**, 12637.
- 36 L. Zhang, J. J. Liang, Y. Huang, Y. F. Ma, Y. Wang and Y. S. Chen, *Carbon*, 2009, **47**, 3365.
- 37 H. A. Becerril, J. Mao, Z. Liu, R. M. Stoltenberg, Z. Bao and Y. Chen, *ACS Nano*, 2008, **2**, 463.
- 38 Y. Gogotsi and P. Simon, *Science*, 2011, **334**, 917.
- 39 M. D. Stoller and R. S. Ruoff, *Energy Environ. Sci.*, 2010, **3**, 1294.
- 40 Y. F. Tang, L. Yang, Z. Qiu and J. S. Huang, *Electrochem. Commun.*, 2008, **10**, 1513.
- 41 L. Tang, Y. Wang, Y. Li, H. Feng, J. Lu and J. Li, *Adv. Funct. Mater.*, 2009, **19**, 2782.
- 42 Y. He, L. Huang, J. S. Cai, X. M. Zheng and S. G. Sun, *Electrochim. Acta*, 2010, **55**, 1140.
- 43 H. Liu, G. Wang, J. Wang and D. Wexler, *Electrochem. Commun.*, 2008, **10**, 1879.
- 44 T. Muraliganth, A. V. Murugan and A. Manthiram, *Chem. Commun.*, 2009, 7360.
- 45 J. Z. Wang, C. Zhong, D. Wexler, N. H. Idris, Z. X. Wang, L. Q. Chen and H. K. Liu, *Chem.-Eur. J.*, 2011, **17**, 661.
- 46 J. Su, M. Cao, L. Ren and C. Hu, *J. Phys. Chem. C*, 2011, **115**, 14469.
- 47 P. H. Klug and E. L. Alexander, *X-ray Diffraction Procedures for Poly-crystalline and Amorphous Materials*, John Wiley & Sons, New York, 1974.
- 48 L. G. Cancado, K. Takai, T. Enoki, M. Endo, Y. A. Kim, H. Mizusaki, A. Jorio, L. N. Coelho, R. Magalhães-Paniago and M. A. Pimenta, *Appl. Phys. Lett.*, 2006, **88**, 163106.
- 49 Y. Zhu, S. Murali, M. D. Stoller, K. J. Ganesh, W. Cai, P. J. Ferreira, A. Pirkle, R. M. Wallace, K. A. Cychoz, M. Thommes, D. Su, E. A. Stach and R. S. Ruoff, *Science*, 2011, **332**, 1537.
- 50 C. Liu, Z. Yu, D. Neff, A. Zhamu and B. Z. Jang, *Nano Lett.*, 2010, **10**, 4863.
- 51 Y. Wang, Z. Hong, M. Wei and Y. Xia, *Adv. Funct. Mater.*, 2012, **22**, 5185.
- 52 Q. Wang, Z. Wen and J. Li, *Adv. Funct. Mater.*, 2006, **16**, 2141.
- 53 Z. Chen, V. Augustyn, J. Wen, Y. Zhang, M. Shen, B. Dunn and Y. Lu, *Adv. Mater.*, 2011, **23**, 791.
- 54 A. D. Pasquier, I. Plitz, S. Menocal and G. G. Amatucci, *J. Power Sources*, 2003, **115**, 171.